Spectral signs of aeolian activity around a sand-dune belt in northern Algeria

Mohamed Hassani[a], Djouher Saadoud[b], Moulley Charaf Chabou[a], Francisco José Martín-Peinado[c], Manuel Sánchez-Marañón[c*]

[a] Institute of Architecture and Earth Sciences, Department of Earth Science, Ferhat-Abbas University, Sétif, Algeria.

[b] Faculty of Earth Sciences, Geographical and Territorial Amenagement, Houari Boumediene University of Sciences and Technology, Algiers, Algeria.

[c] Department of Soil Science and Chemical Agriculture, University of Granada, 18071 Granada, Spain.

*Corresponding author: msm@ugr.es

Abstract

Past work on dunes has used color to investigate the provenance, stabilization, and age of the sand. Instead, we look for signs of aeolian activity in the colors of a sand-dune belt in northern Algeria. On the one hand, visible and near-infrared spectral analyses of satellite images and laboratory samples showed reddish, yellowish, and whitish sands, depending on the amount of gypsum particles and Fe oxides coating quartz grains. Specifically, the dithionite-extractable Fe content was related to a redness index calculated from remote-sensing data ($R^2 = 0.80$) and the abundance of hematite, estimated in the second derivative of the Kubelka-Munk function, paralleled the CIELAB hue-angle of sand samples ($R^2 = 0.91$). On the other hand, a spatiotemporal analysis showed that the reddish sand had undergone a continuous remobilization and dispersion throughout the area, reaching two large sabkhas with seasonal water. Yellowish and whitish sands appeared as patches on the periphery of these sabkhas and along the dune belt, exhibiting percussion marks and dissolution pits on the surface of quartz grains. Taken together, the results suggest that the reddish sand partially loses its Fe-oxide coatings by mechanical abrasion in the entrainment and reductive dissolution in the sabkhas during waterlogging, becoming yellowish. The periodic reactivation by wind of reddish and yellowish grains, together with whitish gypsum particles formed by evaporation as the sabkhas dry up, may explain the sorting of grains according to their mineralogy and size along the sand-dune belt, resulting in striking color changes. Accordingly, color reflects sand movements and chemical processes taking place in this dune system.

Keywords: Dunes, Remote sensing, VIS-NIR spectra, Color, Fe content.

1. Introduction

Aeolian sand dunes, considered as emergent dynamical systems that result from the interaction of sand and wind, constitute one of the main research challenges in arid and semi-arid geomorphology (Goudine, 2013; Lorenz and Zimbelman, 2014). Therefore, a plethora of field studies concerning wind flow and sand flow, experimental simulations with wind tunnels, numerical models that reproduce shape patterns observed in nature, and chronological approaches of the formation phases have been conducted to elucidate how dunes are created and maintain their shape (Livingstone et al., 2007; Durán et al., 2010; Alappat et al., 2017, Lämmel et al., 2018). Remote sensing and spatial analysis were also recommended to document the evolution of dunes (Hugenholtz et al., 2012). These technologies enable the examination and quantification of the shape, mobility, patterns, and hierarchies of dunes, as well as the detection of surface changes in the redistribution of sand grains (Necsoiu et al., 2009; Levin, 2011; Gadhiraju et al., 2014, Shumack et al., 2017; Afrasinei et al., 2018). In addition, from the visible and near-infrared spectral information contained in the images, the authors have interpreted the chemistry, mineralogy, and grain size of dune sands (Howari et al., 2007; Ghrefat et al., 2007; Hubbard et al., 2018). Exploiting spectral information of these terrestrial landforms is also important to improve our understanding of the operation of aeolian processes on other planetary surfaces (Lapotre et al. 2017).

Much of the spectral analysis in dunes has focused on the visible region using some bands then combined as color indices. For example, surface reddening of dunes was examined in the Namib Desert (White et al., 1997) and the Rub'Al Khali Desert (White et al., 2001) with Landsat TM images. More recently, as portable measurement equipment has become more available, considerable progress has been made in quantifying and mapping the reddening patterns of dunes using field and laboratory spectroscopy methods (Bullard and White, 2002; Levin et al. 2007a), airborne hyperspectral sensors (Ben-Dor et al., 2006), and simple digital cameras (Levin et al. 2005), as well as by combining laboratory spectra with remote-sensing data (White et al., 2007, Adnani et al., 2018). All these works have stated that the coloring process in desert dunes and coastal dunes was related to an increase over time of secondary Fe-oxide minerals coating the sand grains. Consequently, dunes become yellower or redder as their age and stability increase. Redness indices have been used to evaluate this as well as the source and transport paths of the sand grains. However, some circumstances within a dune system may disrupt these relationships, such as the presence of inter-dune freshwater ponds, where anaerobic conditions may cause Fe reduction and thereby bleach the sand forming the dunes (Levin et al., 2007b). Sand abrasion has also been proposed as a way by which the Fe coatings are at least partly lost, leading to the whitening of sand grains (Bullard et al., 2004; Bullard and White, 2005).

Therefore, spectral color appears to respond well to the aeolian processes involved in the development of a dune system, including the sand availability and the dynamism of sand grains from the supply area to their place of accumulation. The idea is consistent with the contention that dune activity may lead to active morphological changes (Hugenholtz et al., 2012), with color being one of the most evident morphological characteristics of sand grains which is also related to their composition, size, and morphology (Baranoski et al., 2014). However, beyond using a few spectral bands, sometimes combined in an index, the color quantification requires the consideration of the entire visible spectrum and physical methods of color expression. In this way, from diffuse reflectance spectra converted in the Munsell codes (ASTM, 2008), CIELAB parameters (CIE, 2004), and second derivative of the Kubelka-Munk function (Scheinost et al., 1998), many authors have reported on the reliability of color to identify and quantify the different types of Fe oxides and not only their total amount (Scheinost and Schwertmann, 1999; Martín-Garcia et al., 2016). By extension, soil-formation processes involving these minerals have been investigated from color data (Sandler et al., 2015; Sánchez-Marañón et al., 2015). However, this colorimetric approach has not yet been tested in dune studies.

The present study arose from the observation of different colors along a sand-dune belt and its surrounding area in the Zahrez depression of Algeria. Our objective was to determine whether a spectral and colorimetric analysis could provide signs or indications of the activity and functioning of this dune system. The spectral information would be checked and supported by analyses of composition, size, and morphology of the sand grains.

2. Materials and methods

2.1. Location

The study area is the Zahrez depression within the Algerian steppe (Fig.1), an alluvial depression with a gentle slope (5%) between two parallel limestone mountains of the Saharan Atlas running SW-NE. In addition to some dry river beds, two desert salt lakes or sabkhas alternate between waterlogging and evaporation. Further south, parallel to the mountains, rises a spectacular sand-dune belt more than 150 km long, about 4 km wide, and on average 15 m high. In this setting, with frequent inter-dune spaces, the dunes take on different forms, including barchan, parabolic, seif, and sandy-sail shapes.

The climate is semi-arid with very dry summers (ONM, 2014). The mean temperature in summer of 38°C drops to 6°C in winter. The annual mean rainfall is 285 mm. During winter and spring, the wind frequently blows from the west and northwest (30% of the time) with an average speed of 16.6 m/s. In summer and autumn, the wind also blows mainly from the west and sometimes from the south. The southerly direction corresponds to the Sirocco, which is a hot and dry wind coming from the Sahara for an average period of 59 days. The aridity reduces the vegetation to a sparse steppe dominated mainly by *Aristida pungens* L. and *Atriplex halimus* L.

2.2. Remote sensing

2.2.1. Image preprocessing

We acquired Landsat-5 TM images, two from 1987 and two from 2007, in addition to two Landsat-8 OLI images from 2016, a Sentinel-2A image (S-2A) from 2016 and a Hyperion image from 2004 (Table 1). The latter covers only a small part of the area (Fig. 1). Using ENVI *v*.5.2 (Exelis Visual Information Solutions, Boulder, CO, USA), the pairs of TM and OLI images of each year were merged into a scene and their spectral bands resampled with the Gram-Schmidt spectral sharpening method to a spatial resolution of 15 m (Laben and Brower, 2000). We also resampled the S-2A bands to 15 m, except b1, b9, and b10 with low spatial resolution (60 m, Table 1), and b7 and b8a with high sensitivity to aerosols, water vapor, and cirrus detection. Because OLI and S-2A images were acquired on a similar date, we also blended seven bands of the OLI image (b1 to b7, Table 1) and seven of the S-2A (b2 to b6 besides b11 and b12) into a single multispectral image of 14 bands (henceforth OLI + S-2A). In the Hyperion image, 92 of its 242 bands were removed for the reasons listed in Table 1. Finally, the Digital Number values of the bands were converted to Top of Atmosphere spectral radiance and this in turn was subsequently transformed to reflectance data atmospherically corrected by Fast Line-of-Sight Atmospheric Analysis of Spectral Hypercubes (Berk et al., 1998; Pour et al., 2014).

2.2.2. Image processing

To determine endmembers, we first used the Minimum Noise Fraction transformation (Green et al., 1988). This is two cascaded principal components in ENVI software. The first transformation estimates the noise in the data and the second is a standard transformation of the noise-whitened data. The resulting bands of the transformed data are ranked with most of the surface-reflectance variation in the first few components. The bands containing only noise and giving no coherent images were not subsequently processed. In the second step for determining endmembers, we looked for spectrally pure pixels, placing them in an *n*-dimensional scatter plot for a clustering analysis (*n* = number of bands), which develops individual endmember spectra. These were compared with spectra of standard materials of the ASTER spectral library (Baldridge et al., 2009) using Mixture-Tuned Matched Filtering (Boardman et al., 1995). In the Hyperion image, we applied the technique Sequential Maximum Angle Convex Cone in order to find spectral endmembers and the classification method Spectral Angle Mapper to assign them to specific materials of the ASTER library.

From the processed satellite images, we also calculated Redness Index (RI, Mathieu et al., 1998) and Modified Soil Adjusted Vegetation Index (MSAVI, Qi et al., 1994) with the equations:

$$RI = \frac{\rho_r^2}{\rho_b \times \rho_g^3} \qquad (1)$$

$$MSAVI = \frac{(1 + L)(\rho_{nir} - \rho_r)}{\rho_{nir} - \rho_r + L} \qquad (2)$$

where, ρ_r, ρ_g, ρ_b, and ρ_{nir} represent the reflectance at the wavelength range of red, green, blue, and near-infrared, whereas L is an adjustment parameter to minimize the dependent effects of surface conditions. The MSAVI is recommended to eliminate from the satellite images the vegetation effects in arid and semi-arid regions (Funk et al., 2014).

2.3. Sand samples

After analyzing the RGB color of satellite images, we designed a field judgment sampling to collect a total of 27 sand samples. Most of the samples were taken along the entire sand-dune belt and some in the surrounding area, which showed a more uniform aspect in the images (Fig. 1). The sampling points were positioned by a portable GPS with UTM geographic coordinate system. Around each point, a sample of about 1 kg was composited after mixing sand from the upper 5 cm of three different pits, in order to get one representative sample. In addition, for comparison with the sands of the study area, we took three sand samples (S28, S29, and S30) from the Algerian Sahara collected in Ghardaïa (31º19’N 3º31’E), Hassi R’Mel (32º47’N 3º3’E), and Hassi Messaoud (31º12’N 6º19’E), respectively.

2.4. Spectral measurements in the laboratory

The spectral reflectance of samples collected in the field was recorded using a LabSpec 5100 spectrophotometer in the 350-2500 nm range with resolution of 3-6 nm and sampling every 1 nm (ASD Inc., Boulder, Co. USA). We put five grams of air-dried sand inside cylindrical polyethylene containers 6 cm high and 2 cm in diameter, with top access for introducing a bifurcated probe of optical fiber through which the sample and the instrument were brought into contact. For each sample, the baseline was calibrated using a Spectralon white reflectance standard and 10 measurements were taken and averaged to present its mean spectrum. Subsequently, the continuum-removed spectrum, which is the original spectrum divided by a convex curve fit over the top of the spectrum connecting local maxima with straight-line segments, was calculated with ENVI *v.* 5.2. The resulting continuum-removed spectrum is equal to 1.0 where the convex curve and the spectrum match and less than 1.0 where absorption features occur (Clark et al., 1987). We finally computed the depths and areas of the absorption features (Grove et al., 1992).

The diffuse reflectance (*R*) was also measured with a Minolta CM-2600d spectrophotometer (Minolta, Tokyo, Japan). This instrument has an illuminating/viewing geometry diffuse/8º, recording the light reflected by the sample with the specular component excluded between 360 and 740 nm at 10-nm intervals. After the sand was placed in shallow cylindrical containers 15 mm in diameter and 5 mm deep with the upper surface open and leveled, measurements were made in triplicate putting the measuring port of our device with a target mask of 50 mm^2 directly on the surface of sand samples. We used the Spectramagic program supplied with the instrument to calculate from the reflectance spectra the Munsell color codes *hue*, *value,* and *chroma* under C illuminant and CIE 1931 Standard Observer (ASTM, 2008), as well as CIELAB color coordinates L^* (0-100 lightness scale), a^* (red $+a^*$ green $-a^*$ scale), b^* (yellow $+b^*$ blue $-b^*$ scale), C^*_{ab} (chroma), and h_{ab} (hue-angle) under D65 illuminant and CIE 1964 Standard Observer (CIE, 2004). Finally, from the reflectance values R, the wavelength-dependent Kubelka-Munk function (ratio of absorption K to scattering S) was expressed as:

$$\frac{K}{S} = \frac{(1-R)^2}{2R} \qquad (3)$$

Continuous K/S data vs. wavelengths were plotted in the OriginPro v. 7.5 program (OriginLab Co, MA, USA) to find the second-derivative curve. In this way, the resolution of K/S curves can be enhanced in order to find the position (minima values) of absorption bands (Scheinost et al., 1998) produced by electronic transitions, which identify certain minerals according to the crystal field theory (Burns, 1993).

2.5. Analysis of size, mineralogy, and morphology of the sand grains

In the sand samples collected in the field, after removing organic matter with H_2O_2 and dispersion with hexametaphosphate, particle size was determined by sedimentation (pipette method) for silt and clay and wet sieving for sand, in order to determine the USDA textural classes (Soil Science Division Staff, 2017). Once the sand dried for 24 h in an oven at 80°C, we sieved the fractions of very coarse (2.0-1.0 mm), coarse (1.0-0.5 mm), medium (0.5-0.25 mm), fine (0.25-0.10 mm), and very fine grain size (0.10-0.05 mm). From their percentages by weight, the four principal moments mean size (Mz), sorting (σ_I), skewness (Sk_I), and kurtosis (K_G) were calculated according to the criteria of Folk and Ward as described in the Gradistat program (Blott and Pye 2001).

Five grams of selected sand samples were also ground in an automatic agate mortar over 10 min to determine their mineralogy by X-ray diffraction (XRD) in unoriented powder. We scanned the powder samples with a Philips X'Pert PWR diffractometer, using CuKα radiation (wavelength, $\lambda = 0.15406$ nm) at 40 kV and 40 mA, angular interval from 5º to 90º with 0.02º 2θ steps, and 4s counting time per step. Minerals were identified from the diffractograms by analyzing the position, intensity, shape, and width of the peaks. Semi-quantitative estimates of their proportions were also made on the basis of the intensity factors method. Because the Fe-oxide coatings were diluted in the sand fraction, we also used atomic absorption spectrophotometry to measure in all samples the amount of citrate-dithionite extractable iron (Fe_d) (Holmgren, 1976).

Finally, the morphology of sand grains was studied in selected samples. First, we examined the size distribution, shape, and color of grains under a binocular magnifying glass. Then, some quartz grains were randomly separated from each sample. Intact grains and washed grains treated with a 15% hydrochloric acid solution for removing iron oxides (Vos et al., 2014) were fixed to a holder with colloidal silver, metalized with carbon in two orientations diverging 20-30º, and analyzed by scanning electron microscopy (SEM). We used a Zeiss SUPRA40VP apparatus (ZEISS Co., Germany) with an acceleration voltage of 30 kV and nanometric resolution, in conventional mode of secondary electrons and backscattered electrons. For the elemental microanalysis of grains, an energy-dispersive X-ray (EDX) spectrometer was connected to the SEM, model AZTEC 2.4 (Oxford instruments, UK), in pinpoint mode (diameter 1 μm), resolution of 10 eV/ch, and a spectrum reaching time of 100 s.

3. Results

3.1. Spectral endmembers and redness index from satellite images

Once the raw images of remote sensing acquired in 2016 were mosaicked and their spectral bands resampled, we delimited the area shown in Fig. 1. The results of applying the Minimum Noise Fraction (MNF) transformation to the multispectral bands (Fig. 2) revealed that a small group of MNF bands explains most of the spatial variability, both in the OLI and S-2A images and in our combined proposal OLI + S-2A. The latter, however, had greater eigenvalues in the first few MNF bands and consequently better spectral information than the OLI and S-2A data individually. Therefore, in the subsequent processing of spectral data, we included the first eight MNF bands of OLI + S-2A whose eigenvalues were above the break in slope of the eigenvalue plot (Fig. 2).

The Mixture-Tuned Matched Filtering (MTMF) analysis considering the ASTER standard library found six individual spectral endmembers, which matched with reddish-brown fine sandy loam, light-yellowish-brown loamy sand, white gypsum dune sand, gypsum, dry sediments, and wet sediments. Fig. 3 shows the spatial distribution of the first three endmembers corresponding to sand of different colors: reddish, yellowish, and whitish. The sand-dune belt was evident along the southern boundary of the area. According to this satellite approach, the whitish sand (blue in Fig. 3) appeared mostly in the northeast half of the dune belt. The yellowish sand appeared in the southwest part of the dune belt, as well as partially surrounding the whitish sand core and also accumulated together with whitish sand in patches of different sizes on the periphery of the sabkhas. The reddish sand spread throughout the flat and gently sloping areas surrounding the dune belt, being especially abundant north of the entire belt. Finally, the endmember gypsum and sediments were part of the two sabkhas shown in black in Fig. 3.

From the Hyperion hyperspectral image (Fig. 4a), the Sequential Maximum Angle Convex Cone (SMACC) technique on the inverted MNF image revealed 8 endmembers. According to the classification method Spectral Angle Mapper (SAM), three of the eight (endmembers 4, 1, and 8; Fig. 4b) matched with the ASTER standards reddish-brown fine sandy loam, light-yellowish-brown loamy sand, and white gypsum dune sand. Consequently, the sand endmembers shown in the SAM map were the same as those of the MTMF map derived from OLI + S-2A (Figs. 4b and 4c). In addition, even though the Hyperion and OLI + S-2A data differed in spectral resolution (150 bands *vs.* 14 bands), acquisition date (2004 *vs.* 2016), and processing technique (SAM *vs.* MTMF), the spatial distribution of sand endmembers proved to be more or less similar in both maps (Figs. 4b and 4c). Therefore, the SAM results from the Hyperion image validate the mapping of reddish, yellowish, and whitish sands performed with OLI + S-2A data and MTMF technique throughout the study area (Fig. 3).

Finally, we calculated the redness index (RI, Eq. 1) in three temporary moments using Landsat TM images of 1987 and 2007 and Landsat OLI images of 2016. Once the vegetation effects were corrected with MSAVI (Eq. 2), the RI values ranged between 0 and 310. The RI maps varied from one year to the next (Figure 5) and, considering RI greater than 65 as reddish sand, the difference between maps showed spatiotemporal changes in the distribution of reddish sand.

3.2. Spectra of the sand samples

The visible and near-infrared spectra of 30 sand samples taken in the field for testing in the laboratory the three spectral endmembers determined by remote sensing are shown in Figure 6a. Like the ASTER standard for white gypsum dune sand, the spectra of samples S1, S2, S5, S11, and S13 (whitish sand in Figure 6a) show high reflectance in the range 600-1100 nm and strong absorption bands close to 1450 nm, 1750 nm, 1950 nm, and 2250 nm. Samples collected from the endmembers light-yellowish-brown loamy sand (yellowish sand) and reddish-brown fine sandy loam (reddish sand) had, also like their ASTER standards, high reflectance in the range 900-2100 nm and low-intensity absorption bands close to 1400 nm, 1900 nm, and 2200 nm. These spectra showed very similar shapes, but reddish sand samples had lower reflectance values and a steeper slope between 500 and 600 nm than yellowish sand samples. The continuum removal transformation (Figure 6b) confirmed three groups of samples well separated by an absorption feature close to 500 nm. However, reddish and yellowish samples were indistinguishable in the near infrared.

Because the visible spectral region differentiated the three sample groups better than did the near-infrared range, additional spectral-color measurements were recorded. Diffuse reflectance curves (Fig. 7a) showed that samples outside the sand-dune belt (e.g. S10, S25, and S26, Fig.1), including those of the Algerian Sahara (S28, S29, and S30), had lower reflectance over the entire range of wavelengths and a steeper absorption edge (between 540 nm and 600 nm) than those inside the sand-dune belt (e.g. S12, S16 and S17). This resulted in redder (lower h_{ab}) and darker (lower L^*) samples outside the sand-dune belt (Table 2 and Fig. 1), whereas the inside samples turned yellowish (higher h_{ab}). Some samples from the core of the sand-dune belt even became less chromatic (lower a^*, b^* and C^*_{ab}) and lighter (higher L^*) in the northeast (S1, S2, S5, S11, S13), indicating whitish colors.

To find the position and intensity of the absorption bands that caused the sand color, we calculated the second derivative of the Kubelka-Munk function (Fig 7b). Three minima around 420 nm, 480 nm, and 540 nm, and three maxima around 450 nm, 500 nm, and 580 nm were well defined in the resulting curves. All samples showed the second-derivative minima in the same position, indicating the same absorption bands, although their intensity was greater in the relatively more reddish samples (Munsell *hue* < 7.5YR, Table 2) than the yellowish (7.5YR to 8.5YR) and whitish ones (*hue* > 8.5YR and *value* > 7.1).

3.3. Size, mineralogy, and morphology of the sand grains

The USDA textural classes of the samples were sand and loamy sand (< 17% of silt + clay), corresponding primarily to sand-sized grains with some silt and clay in the reddish samples. According to the Gradistat results (Table 3), the mean grain size (*Mz*) of the whitish samples ranged between 3 and 2 phi units, corresponding to fine sand (100-250 µm), whereas in the yellowish and reddish samples varied between 3.2 to 1.1 phi units, with more than half of the samples proving to be medium sand (250-500 µm). The standard deviation (σ_I) was 0.814 phi units in the reddish samples, 0.764 phi units in the yellowish ones, and 0.672 in the whitish ones, indicating size distributions moderately sorted to moderately well sorted, with a progressive decline in the size dispersion around the average. One third of the samples had skewness values (Sk_I) of between +0.1 to -0.1, corresponding to symmetric distributions, and kurtosis values (K_G) greater than 0.9 phi units, i.e. a high concentration of grains relative to the average size. Finally, the steep cumulative distribution curves indicate narrow ranges of sand sizes, although variable among samples (Fig. 8). In general, 90% of grains were between 1000 µm and 250 µm in reddish samples, between 375 µm and 125 µm in yellowish samples, and between 375 µm and 50 µm in whitish samples.

The XRD analysis (Table 3) identified quartz as the dominant mineral, which ranged between 83% and 98% in the reddish and yellowish sands and between 63% and 74% in the whitish ones. The latter also had gypsum (22-35%). Feldspars, calcite, and dolomite were in minor contents. In addition, a remarkable variability of the dithionite-extractable iron (Fe_d) content was measured in all samples (Table 3), the mean values of reddish (416.7 ± 152.8 mg kg^{-1}), yellowish (210.1 ± 116.8 mg kg^{-1}), and whitish (45.8 ± 21.3 mg kg^{-1}) samples being significantly different ($P < 0.001$).

Under binocular microscopy, virtually all grains from the reddish and yellowish samples had a roughly rounded shape, although with a more translucent and polished look in the yellowish ones (Fig. 9a, b). However, in the whitish samples, together with rounded quartz grains, angular, subangular and flat elongated particles also appeared that could be gypsum (Fig. 9c). With SEM, the quartz grains exhibited materials precipitated on their surface as illustrated by the brighter parts of the backscattered electron images (Fig. 9d). Unlike the uncoated areas, where the EDX pintpoint spectra showed only the peaks for Si and O (Fig. 9e), the precipitates contained a high percentage of Fe atoms (Fig. 9f), which, in agreement with the Fe_d results, indicate the presence of Fe oxides. Once the grains were cleaned with the HCl solution, all showed morphologies such as meandering ridges, dish-shape concavities, and several V-shaped indentations, suggesting percussion between grains. In addition, the quartz grains from the reddish samples showed high relief with topographically irregular surfaces and large concavities filled by precipitated silica droplets (silica globules, Fig. 9g). On the contrary, the grains of the dune belt exhibited more polished surfaces with corrosion holes and large groove-shaped etched incisions (solution pits and crevasses, Fig. 9h, i).

4. Discussion

We have verified by SEM and EDX microanalysis the presence of precipitated Fe forms on the quartz grains (Fig. 9d-f). Their content measured as dithionite-extractable Fe (Fe_d, Table 3) varied in parallel to the redness index of the satellite images (Fig. 10a) and to the intensity of the absorption band at ~500 nm of the laboratory spectra (Fig. 6b and Fig. 10b). The spectra also showed near-infrared absorption bands of hydration water and hydroxyl vibrations (OH stretching overtone at ~1400 nm and combined OH stretching and bending at ~1900 nm and ~2200 nm), mostly of low intensity that could be attributed to small amounts of goethite and silt- and clay-sized phyllosilicates (Bishop et al., 2008; Cuadros et al., 2016). However, these bands became more intense in some spectra with characteristic and distinct triplet bands near 1400-1500 nm, a strong band at 1950 nm, and multiple features near 2200-2300 nm, indicating the presence of gypsum (Clark et al., 2007; Bishop et al., 2014), also confirmed by XRD (Table 3). Consequently, the spectral data were taken as evidence of variable contents of Fe_d and gypsum in the colored sands (Fig. 3).

Due to the progressive decline in Fe_d and incorporation of gypsum (Table 3), as proved in soil-color studies (Sánchez-Marañon et al., 2015), spectral curves can gain in reflectance along the entire visible region and lose the steep absorption edges (Fig. 7a). Thus, the CIELAB color parameters h_{ab} and L^* progressively increase (less red and lighter, Table 2) while a^*, b^*, and C^*_{ab} decrease (less chroma). In general, the Fe oxides are responsible for the redness of dunes (Mathieus et al., 1998; White et al., 2007; Levin et al., 2007a) and specifically in our study, the color changes could be attributed to different contents in goethite and hematite. Both minerals were unambiguously detected by the absorption bands at 480 nm and 540 nm in the *K/S* second derivative (Scheinost et al., 1998). In addition, according to the amplitudes in the derivative curves between 420 nm (minimum) and 450 nm (maximum) and between 540 nm (minimum) and 580 nm (maximum), which are spectral indices of the abundance of goethite and hematite (Martín-García et al. 2016), respectively, both Fe oxides decrease from the reddish to yellowish and whitish samples (Fig. 7b). In addition, the relation of these Fe minerals with h_{ab} indicates that hematite had more influence on the redness of samples ($R^2 = 0.91$, Fig. 10c), in agreement with its red hue vs. the yellow of goethite (Sánchez Marañón et al., 1997; Scheinost and Schwertmann, 1999; Adnani et al., 2018).

The reddish samples located in the alluvial depression (e.g. S25 and S26), in the southwestern end of the sand-dune belt (e.g. S22), and in inter-dune positions (e.g. S18) had spectral characteristics very similar to those of the Algerian Sahara sands (S28, S29, and S30, Table 2 and Figs. 6 and 7), indicating that all of them are loaded of goethite and hematite covering the quartz grains. This spectral similarity also suggests a Sahara provenance of the reddish sands, at least in part, which agrees with the wind regime in the area that blows mainly from the west together with the southern sirocco. If not, in any case, the reddish sands appear to have an aeolian origin, whose enrichment in Fe oxides has been seen as a sign of old age and long transport (White et al., 2001; Levin et al., 2007a, b). Rounded quartz grains with collision and abrasion marks (Fig. 9g) typical of the aeolian environments (Vos et al., 2014) also support our spectral interpretation. Alluvial sediments, soil materials, and Saharan dust may also be part of these reddish materials, which are mainly sandy but with some silt and clay. Their spatiotemporal spectral analysis (Fig. 5) showed that they have been moving and constantly changing their position with a stronger dynamism in the southwestern half of the area compared to the northeastern half.

Yellowish and whitish sands, on the contrary, are more confined to the dune belt (Fig. 3). However, taking into account their spectral features, it is difficult to envisage, especially for yellowish sand, an independent origin and development of the reddish sand. In fact, although the satellite approach distinguished yellowish sand along the margins of the entire belt and centre of the dunes in the western half, some samples taken there (e.g. S21, S22, S23) were only slightly less reddish than the scattering sand of depression (Table 2). Overall, in addition, the second derivatives of *K/S* curves (Fig. 7b) indicate the same absorption bands, although of lower intensity in the yellowish samples due to a decrease in Fe oxides. Because the reddish sand is redistributed according to the wind flow (Fig. 5), its continuous entrainment could have caused a partial loss of the coatings, especially the reddish hematite, which makes the grains yellower. Deferrification of sand grains by mechanical impact (Bullard and White, 2005) and/or chemical dissolution (Levin et al., 2007b) is not uncommon in aeolian environments.

In particular, reductive dissolution, by far the most important natural dissolution mechanism of Fe oxides also reproduced in laboratory (Roden et al., 2000), as well as the formation of soluble complexes of Fe(II) and Fe(III) with chloride and sulfate (Cornell and Schwertmann, 2003) seem possible in the study area because of the two big sabkhas with seasonal saline water (Fig. 1). Evidence consists of pockets of yellowish sand on the edges of these sabkhas (Fig. 3), indicating that originally reddish grains, once under water, may turn yellow by preferential dissolution of hematite (red) over that of goethite (yellow), a process termed xanthization (Nehren et al., 2016). This was also demonstrated *in vitro* (Jeanroy et al., 1991) and it is in accordance with the sequence in reducibility by Fe-reducing bacteria under O_2-free conditions (Cornell and Schwertmann, 2003). Thus, yellowish grains can then be exposed on the surface as the sabkhas dry up. Due to seasonal contrasts, the grains may undergo several depigmentation cycles before being reactivated by the wind. This might be the case of whitish quartz sand, whose distinct etching features (Fig. 9i) confirmed that these grains have been subjected to dissolution process favored by alkaline conditions and high temperatures (Brantley et al., 1986; Gratz et al., 1990). The quartz grains of whitish sand look similar in color to those of yellowish sand (Fig. 9 b,c) but the addition of gypsum, seemingly formed by evaporation in the sabkhas during dry seasons, catalyzes the sand whitening.

Finally, the color changes along the sand-dune belt indicate a whitening in direction SW-NE, which is consistent with a decrease in size (Table 3, Fig. 8) and density (less Fe-oxide coating on quartz and more gypsum) of the grains in the wind direction (Adnani et al., 2018; Hubbard et al., 2018). The color arrangement could also be influenced by the possible entry of reddish sand and its greater dynamism in the western half, as well as by the proximity of the gypsum source (sabkha) to the eastern half of the sand-dune belt.

5. Conclusions

The spectral and colorimetric data from satellite images and samples measured in the laboratory show dune sands with different amounts of Fe-oxide coatings and gypsum particles, which give rise to sand colors that go from reddish to yellowish and whitish. A spatiotemporal analysis of spectral redness also reveals that the reddish sand has been continuously remobilized by the wind reaching the sabkhas. On the way and after the waterlogging, part of the Fe-oxide coatings could be removed by abrasion and reductive dissolution. The dissolution of hematite causes a loss of redness. This, together with the addition of gypsum formed by evaporation during the dry season, can explain the development of yellowish and whitish sands from reddish sand. Evidence is the appearance of patches of yellowish and whitish sands on the periphery of the sabkhas as they dry up, as well as the percussion cracks and etchings on the surface of their quartz grains. Finally, the grains are well sorted according to their composition and size along the sand-dune belt in parallel with color changes from the reddish to yellowish and whitish. Because the color of sand depends on its composition, which changes by the action of the processes taking place in the dune system, we conclude that the color changes are spectral signs of activity and dynamic connections between the sands. Accordingly, colorimetric approaches can improve our understanding of the operation of aeolian processes.

Acknowledgment

This work was supported by the Ministry of Economy and Competitiveness of the National Government of Spain (research project FIS2016-80983-P) with assistance from European Regional Development Fund (ERDF). MH is grateful for the financial support of the Algerian Ministry of Higher Education and Scientific Research through the PNE Program (2016-2017).

References

Adnani, M., Azzaoui, M.A., Elbelrhiti, H., Ahmamou, M., Masmoudi, L., 2018. Investigation of reddening patterns of dune sands – The megabarchans of Al-ghord Lahmar (Khnifiss National Park, south-west of Morocco). Catena 162, 230-244.

Afrasinei, G.M., Melis, M.T., Arras, C., Pistis, M., Buttau, C., Ghiglieri, G., 2018. Spatiotemporal and spectral analysis of sand encroachment dynamics in southern Tunisia. European Journal of Remote Sensing 51, 352-374. DOI: 10.1080/22797254.2018.1439343.

Alappat, L., Joseph, S., Tsukamoto, S., Kaufhold, S., Frechen, M. 2017., Chronology and weathering history of red dunes (Teri Sands) in the southwest coast of Tamil Nadu, India. Zeitschrift der Deutschen Gesellschaft fur Geowissenschaften 168, 183-198.

ASTM, 2008. Standard Practice for Specifying Color by the Munsell System. ASTM International D 1535-08 (PA).

Baldridge, A.M., Hook, S.J., Grove, C.I., Rivera, G., 2009. The ASTER spectral library version 2.0. Remote Sensing of Environment 113, 711–715.

Baranoski, G.V.G., Kimmel, B.W., Chen, T.F., Miranda, E., 2014. Influence of sand-grain morphology and iron-oxide distribution patterns on the visible and near-infrared reflectance of sand-textured soils. IEEE journal of selected topics in applied earth observations and remote sensing, Vol 7, N° 9. Doi: 10.1109/JSTARS.2014.2299813.

Ben-Dor, E., Levin, N., Singer, A., Karnieli, A., Braun, O., Kidron, G.J. 2006., Quantitative mapping of the soil rubification process on sand dunes using an airbone CASI hyperspectral sensor. Geoderma 131, 1-21.

Berk, A., Bernstein, L.S., Anderson, G.P., Acharya, P.K., Robertson, D.C., Chetwynd, J.H., Adler-Golden, S.M., 1998. MODTRAN cloud and multiple scattering upgrades with application to AVIRIS. Remote Sensing of Environment 65, 367–375.

Bishop, J., Lane, M., Dyar, M.D., Brown, A., 2008. Reflectance and emission spectroscopy study of four groups of phyllosilicates: smectites, kaolinite-serpentines, chlorites and micas. Clay Miner. 43, 35-54.

Bishop, J.L., Lane, M.D., Dyar, M.D., King, S.J., Brown, A.J., Swayze, G.A., 2014. Spectral properties of Ca-sulfates: Gypsum, bassanite, and anhydrite. American Mineralogist 99, 2105-2115. DOI: 10.2138/am-2014-4756

Blott, S.J., Pye, K., 2001. Gradistat: a grain size distribution and statistics package for the analysis of unconsolidated sediments. Earth Surface Processes and Landforms 26, 1237-1248. DOI: 10.1002/esp.261

Boardman, J.W., Kruse, F.A., Green, R.O., 1995. Mapping target signatures via partial unmixing of AVIRIS data, in Summaries, Fifth JPL Airborne Earth Science Workshop, Jet Propulsion Laboratory Publ.95-1, 1, 23–26.

Brantley, S.L., Crane, S.R., Crerar, D.A., Hellmann, R., Stallard, R., 1986. Dissolution at dislocation etch pits in quartz. Geochimica et Cosmochimica Acta 50, 2349-2361.

Bullard, J.E., White, K., 2002. Quantifying iron oxide coatings on dune sands using spectrometric measurements: An example from the Simpson-Strzelecki Desert, Australia. Journal of Geophysical Research 107: (B6), 2125. Doi: 10.1029/2001jb000454.

Bullard, J.E., McTainsh, G.H., Pudmenzky, C.A., 2004. Aeolian abrasion and modes of fine particle production from natural red dune sands: an experimental study. Sedimentology 51, 1103–1125.

Bullard, J.E., White, K., 2005. Dust production and the release of iron oxides resulting from the Aeolian abrasion of natural dune sands. Earth Surface Processes and Landforms 30, 95–106.

Burns, R.G., 1993. Mineralogical Applications of Crystal Field Theory. 2nd ed. Cambridge University Press, Cambridge.

CIE, 2004. Publication 15:2004. In: Bureau, C.C. (Ed.), Colorimetry, 3rd ed. (Vienna).

Clark, R.N., King, T.V.V., Gorelick, N.S., 1987. Automatic continuum analysis of reflectance spectra. Proceedings of the Third AIS Workshop, 2–4 June 1987. JPL Publication, vol. 87-30. JPL, Pasadena C, pp. 138–142.

Clark, R.N., Swayze, G.A., Wise, R., Livo, E., Hoefen, T., Kokaly, R., Sutley, S.J., 2007. USGS digital spectral library splib06a: *U.S. Geological Survey*, Data Series 231. http://speclab.cr.usgs.gov/spectral-lib.html

Cornell, R.M., Schwertmann, U., 2003. The Iron Oxides. Structure, Properties, Reactions, Occurrences and Uses. Wiley – VCH Verlag GmbH & Co. KGaA, Weinheim.

Cuadros, J., Michalski, J.R., Dekov, V., Bishop, J.L., 2016. Octahedral chemistry of 2:1 clay minerals and hydroxyl band position in the near-infrared. Application to Mars. Am. Mineral. 101, 554-563.DOI: http://dx.doi.org/10.2138/am-2016-5366

Durán, O., Parteli, E.J.R., Herrmann, H.J., 2010. A continuous model for sand dunes: Review, new developments and application to barchan dunes and barchan dune fields. Earth Surf. Process. Landforms 35, 1591–1600.

Funk, R., Hoffmann, C., Reiche, M., 2014. Methods for quantifying wind erosion in steppe regions. In Novel measurement and assessment tools for monitoring and management of land and water resources in agricultural landscapes of Central Asia (pp. 315–327). Springer International Publishing.

Gadhiraju, S.V., Shah, V., Buddhiraju, K.M., 2014. Segmentation of dessert sand dunes. Remote Sensing Letters 5, 961-970.

Ghrefat, H.A., Goodell, P.C., Hubbard, B.E., Langford, R.P., Aldouri, R.E., 2007. Modeling grain size variations of aeolian gypsum deposits of White Sands, New Mexico, using AVIRIS imagery. Geomorphology 88, 57-68.

Gratz, A.J., Bird P., Quiro, G.B., 1990. Dissolution of quartz in aqueous basic solution, 106-236ºC: Surface kinetics of "perfect" crystallographic faces. Geochimica et Cosmochimica Acta 54, 2911- 2922.

Green, A.A., Berman, M., Switzer, P., Craig, M.D., 1988. A transformation for ordering multispectral data in terms of image quality with implications for noise removal. IEEE Transactions on Geosciences and Remote Sensing, 26(1), 65–74.

Grove, C.I., Hook, S.J., Paylor, E.D., 1992. Laboratory Reflectance Spectra of 160 Minerals, 0.4 to 2.5 Micrometers. JPL Publication, 92-2, 406. Jet Propulsion Laboratory, Pasadena.

Goudine, A.S., 2013. Arid and Semi-Arid geomorphology. Cambridge University Press, 461 p.

Holmgren, G.S., 1976. A rapid citrate-dithionite extractable iron procedure. Soil Sci. Soc. Am. Pro. 31, 210–1.

Howari, F.M., Baghdady, A., Goodell, P.C., 2007. Mineralogical and geomorphological characterization of sand dunes in the eastern part of United Arab Emirates using orbital remote sensing integrated with field investigations. Geomorphology 83, 67–8.

Hubbard, B.E., Hooper, D.M., Solano, F., Mars, J.C., 2018. Determining mineralogical variations of aeolian deposits using thermal infrared emissivity and linear deconvolution methods. Aeolian Research 30, 54-96.

Hugenholtz, C.H., Levin, N., Barchyn, T.E., Baddock, M.C., 2012. Remote sensing and spatial analysis of aeolian sand dunes: A review and outlook. Earth-Science Reviews 111, 319-334.

Jeanroy, E., Rajot, J.L., Pillon, P., Herbillon, A.J., 1991. Differential dissolution of hematite and goethite in dithionite and its implications on soil yellowing. Geoderma 50, 79-94.

Laben, C.A., Brower, B.V., 2000. Process for Enhancing the Spatial Resolution of Multispectral Imagery using Pan-Sharpening. U.S. Patent 6,011,875.

Lämmel, M., Meiwald, A., Yizhaq, H., Tsoar, H., Katra, I., Kroy, K., 2018. Aeolian sand sorting and megaripple formation. Nature Physics 14, 759-765. DOI: 10.1038/s41567-018-0106-z.

Lapotre, M.G.A., Ehlman, B.L., Minson, S.E., Arvidson, R.E., Ayoub, F., Fraeman, A.A., Ewing, R.C., Bridges, N.T., 2017. Compositional variation in sands of the Bagnold Dunes, Gale crater, Mars, from visible-shortwave infrared spectroscopy and comparison with ground truth from the Curiosity rover. Journal of Geophysical Research 122, 2489-2509.

Levin, N., 2011. Climate-driven changes in tropical cyclone intensity shape dune activity on Earth’s largest sand island. Geomorphology 125, 239-252.

Levin, N., Ben-Dor, E., Singer, A., 2005. A digital camera as a tool to measure color indices and related properties of sandy soils in semi-arid environments. International Journal of Remote Sensing 26, 5475–5492.

Levin, N., Kidron, G.J., Ben-Dor, E., 2007a. Surface properties of stabilizing coastal dunes: combining spectral and field analyses. Sedimentology 54, 771-788.

Levin, N., Tsoar, H., Maia, L.P., Sales, V.C., Herrmann, H., 2007b. Dune whitening and inter-dune freshwater ponds in NE Brazil. Catena 70, 1-15. doi:10.1016/j.catena.2006.06.006.

Livingstone I., Wiggs, G.F.S., Weaver, C.M., 2007. Geomorphology of desert sand dunes: A review of recent progress. Earth-Science Reviews 80, 239-257.

Lorenz, R.D., Zimbelman, J.R., 2014. Dune worlds: how windblown sand shapes planetary landscapes. Springer-Verlag Berlin Heidelberg. 308 p.

Martín-García, J.M., Sánchez-Marañón, M., Calero, J., Aranda, V., Delgado, G., Delgado, R., 2016. Iron oxides and rare earth elements in the clay fractions of a soil chronosequence in southern Spain. Eur. J. Soil Sci. 67, 749-762. https://doi.org/10.1111/ejss.12377.

Mathieu, R., Pouget, M., Cervelle, B., Escadafal, R., 1998. Relationships between satellite-based radiometric indices simulated using laboratory reflectance data and typic soil color of an arid environment. Remote Sensing of Environment 66, 17–28.

Necsoiu, M., Leprince, S., Hooper, D.M., Dinwiddie, C.L., McGinnis, R.N., Walter, G.R., 2009. Monitoring migration rates of an active subarctic dune field using optical imagery. Remote Sensing of Environment 113, 2441-2447.

Nehren, U., Kirchner A., Heinrichb, J., 2016. What do yellowish-brown soils and stone layers tell us about Late Quaternary landscape evolution and soil development in the humid tropics? A field study in the Serra dos Órgãos, Southeast Brazil. Catena 137, 173‑190.

ONM, 2014. Office National Météorologique de l'Algérie. Rapport météorologique, Laghouat, Algérie.

Pour, A.B., Hashim, M., Marghany, M., 2014. Exploration of gold mineralization in a tropical region using Earth Observing-1 (EO1) and JERS-1 SAR data: a case study from Bau gold field, Sarawak, Malaysia. Arabian Journal of Geosciences 7, 2393–2406.

Qi, J., Chehbouni., A., Huete, A.R., Kerr, Y.H., Sorooshian, S., 1994. A Modified Soil Adjsuted Vegetation Index (MSAVI). Remote sensing of environment, 48(2): 119-126.

Roden, E.E., Urrutia, M.M., Mann, C.J., 2000. Bacterial reductive dissolution of crystalline Fe (III) oxide in continuous-flow column reactors. Applied and Environmental Microbiology, 66, 1062–1065.

Sánchez-Marañón, M., Delgado, G., Melgosa, M., Hita, E., Delgado, R., 1997. CIELAB color parameters and their relationship to soil characteristics in Mediterranean red soils. Soil Sci. 162, 833-842.

Sánchez-Marañón, M., Romero-Freire, A., Martín-Peinado, F.J., 2015. Soil-color changes by sulfuricization induced from a pyritic surface sediment. Catena 135, 173–183.

Sandler, A., Meunier, A., Velde, B., 2015. Mineralogical and chemical variability of mountain red/brown Mediterranean soils. Geoderma 239–240, 156–167.

Scheinost, A.C., Chavernas, A., Barrón, V., Torrent, J., 1998. Use and limitations of the second-derivative diffuse reflectance spectroscopy in the visible to near-infrared range to identify and quantify Fe oxide minerals in soils. Clay Clay Miner. 46, 528–536.

Scheinost, A.C., Schwertmann, U., 1999. Color identification of iron oxides and hydroxysulfates: use and limitations. Soil Sci. Soc. Am. J. 63, 1463–1471.

Shumack, S., Hesse, P., Turner, L., 2017. The impact of fire on sand dune stability: Surface coverage and biomass recovery after fires on Western Australian coastal dune systems from 1988 to 2016. Geomorphology 299, 39-53.

Soil Science Division Staff, 2017. Soil survey manual. United States Department of Agriculture. Handbook No. 18.

Vos K., Vandenberghe N., Elsen J., 2014. Surface textural analysis of quartz grains by scanning electron microscopy (SEM): From sample preparation to environmental interpretation. Earth-Science Reviews 128, 93–104. http://dx.doi.org/10.1016/j.earscirev.2013.10.013.

White, K., Walden, J., Drake, N.A., Eckardt, F., Settle, J.J., 1997. Mapping the iron oxide content of dune sands, Namibia, using Landsat Thematic Mapper data. Remote Sensing of Environment 62, 30–39.

White, K., Goudie, A.S., Parker, A., Al-Farraj, A., 2001. Mapping the geochemistry of the northern Rub' Al Khali using multispectral remote sensing techniques. Earth Surface Processes and Landforms 26, 735–748.

White, K., Walden, J., Gurney, SD. 2007. Spectral properties, iron oxide content and provenance of Namib dune sands. Geomorphology 86, 219–229.

Table 1. Characteristics and acquisition date of the satellite images Landsat TM, Landsat OLI, Sentinel-2A, and Hyperion. For the latter, the 92 bands eliminated before its spectral analysis are also listed.

Landsat TM		Landsat OLI		GSR[a] (m)	Sentinel-2A		GSR[a] (m)	Hyperion (GSR[a] 30 m)		
Bands	Wavelength (nm)	Bands	Wavelength (nm)		Bands	Wavelength (nm)		Bands	Wavelength (nm)	Description
b1	450–520	b1	435–451	30	b1	443	60	1 to 70	356 to 1058	VNIR
b2	520–600	b2	452–512	30	b2	490	10	71 to 242	852 to 2577	SWIR
b3	630–690	b3	533–590	30	b3	560	10	1 to 7	356 to 406	Not illuminated
b4	760–900	b4	636–673	30	b4	665	10	41	760	Oxygen absorption band
b5	1550–1750	b5	851–879	30	b5	705	20	58 to 76	935 to 902	Not illuminated
b7	2080–2350	b6	1566–1651	30	b6	740	20	77 to 78	912 to 922	Overlap region
		b7	2107–2294	30	b7	783	20	79 to 81	930 to 960	Water vapor absorption band
		b8	503–676	15	b8	842	10	98 to 101	1115 to 1150	Water vapor absorption band
		b9	1363–1384	30	b8a	865	20	120 to 132	1346 to 1467	Water vapor absorption band
					b9	945	60	165 to 182	1800 to 1971	Water vapor absorption band
					b10	1375	60	185 to 187	2002 to 2023	Identified by Hyperion bad band list
					b11	1610	20	221 to 224	2366 to 2395	Water vapor absorption band
					b12	2190	20	225 to 242	2405 to 2577	Not illuminated

[a] GSR: Ground spatial resolution

Satellite	Path Row	Acquisition date	
Landsat TM	195/36	17-08-1987	9:46:11
Landsat TM	196/36	08-08-1987	9:52:07
Landsat TM	195/36	08-08-2007	10:13:31
Landsat TM	196/36	15-08-2007	10:19:38
Landsat OLI	195/36	16-08-2016	10:20:18
Landsat OLI	196/36	23-08-2016	10:26:24
Sentinel-2A		23-08-2016	10:26:22
Hyperion	196/36	13-07-2004	10:16:20

Table 2. CIELAB (L^*, a^*, b^*, C^*_{ab}, h_{ab}) and Munsell (Hue Value/Chroma) color parameters of the sand samples ordered from more to less red according to CIELAB h_{ab}.

Sample [a]	L^*	a^*	b^*	C^*_{ab}	h_{ab}	Hue	Value/Chroma
S30 $_r$	53.97	19.32	30.23	35.88	57.42	5.0YR	5.3/6.1
S29 $_r$	53.25	19.31	30.67	36.24	57.80	5.1YR	5.3/6.1
S25 $_r$	52.66	15.05	26.35	30.34	60.27	6.3 YR	5.2/5.0
S26 $_r$	54.26	14.67	25.83	29.70	60.41	6.3 YR	5.4/5.0
S10 $_r$	58.39	17.96	31.69	36.43	60.46	5.9 YR	5.8/6.1
S28 $_r$	58.84	16.42	30.33	34.49	61.56	6.4 YR	5.8/5.7
S22 $_r$	56.38	14.52	27.28	30.90	61.97	6.8 YR	5.6/5.1
S8 $_r$	56.54	14.21	27.32	30.80	62.52	7.0 YR	5.6/5.1
S27 $_r$	57.13	13.55	26.08	29.39	62.54	7.0 YR	5.6/4.9
S18 $_r$	56.31	13.97	26.90	30.31	62.56	7.1 YR	5.6/5.0
S24 $_r$	57.94	12.12	23.88	26.78	63.08	7.3 YR	5.7/4.4
S14 $_r$	58.16	14.34	28.67	32.06	63.43	7.2 YR	5.8/5.3
S23 $_y$	59.25	12.47	25.24	28.15	63.71	7.5 YR	5.8/4.6
S21$_y$	61.07	13.11	26.67	29.73	63.83	7.5 YR	6.0/4.9
S16 $_y$	58.43	11.59	24.33	26.95	64.53	7.7 YR	5.8/4.4
S17 $_y$	61.78	10.22	21.85	24.12	64.94	7.8 YR	6.1/4.0
S12 $_y$	63.83	12.43	27.20	29.91	65.45	7.8 YR	6.3/4.9
S3 $_y$	61.64	11.52	25.37	27.87	65.59	7.9 YR	6.1/4.6
S9 $_y$	63.70	12.37	27.41	30.07	65.72	7.9 YR	6.3/4.9
S20 $_y$	64.58	12.35	27.49	30.14	65.80	7.8 YR	6.4/4.9
S7 $_y$	61.97	12.06	27.13	29.69	66.03	8.0 YR	6.1/4.8
S4 $_y$	63.95	12.24	27.63	30.22	66.11	8.0 YR	6.3/4.9
S19 $_y$	62.09	11.55	26.40	27.92	66.22	8.1 YR	6.1/4.6
S6 $_y$	64.37	11.94	27.43	29.91	66.47	8.1 YR	6.4/4.9
S15 $_y$	60.58	10.72	25.41	27.58	67.12	8.4 YR	6.0/4.4
S2 $_w$	73.84	6.79	19.31	20.47	70.64	8.9 YR	7.3/3.2
S11 $_w$	72.88	7.16	19.59	20.97	71.08	8.9 YR	7.1/3.4
S1 $_w$	74.80	6.08	18.06	19.06	71.54	9.0 YR	7.4/3.0
S5 $_w$	75.76	5.37	16.81	17.65	72.44	9.2 YR	7.5/2.7
S13 $_w$	76.72	4.66	15.56	16.25	73.35	9.3 YR	7.6/2.5

[a] The subscripts r, y, and w next to the sample label point out relatively reddish, yellowish, and whitish samples, respectively.

Table 3. Grain size statistics, mineralogy, and content of citrate-dithionite extractable iron (Fe_d). Samples were ordered from more to less red according to CIELAB h_{ab}.

	Grain size statistics (phi units)				Mineralogy[b] (%)					
Sample [a]	Mean	Sorting	Skewness	Kurtosis	Q	Fds	Ca	Do	Gy	Fe_d (mg kg^{-1})
S30$_r$	1.50	1.03	0.27	2.96	95.7	2.9	1.4	0.0	0.0	602.7
S29$_r$	1.93	0.74	0.22	1.82	98.1	0.0	1.9	0.0	0.0	590.5
S25$_r$	2.50	0.83	0.00	1.23	n.d.	n.d.	n.d.	n.d.	n.d.	287.0
S26$_r$	3.00	0.66	-0.20	0.85	94.7	4.2	1.1	0.0	0.0	341.3
S10$_r$	2.78	0.98	-0.01	1.13	n.d.	n.d.	n.d.	n.d.	n.d.	282.5
S28$_r$	1.84	0.97	0.50	2.16	98.0	0.0	2.0	0.0	0.0	501.3
S22$_r$	1.50	0.90	0.28	2.00	n.d.	n.d.	n.d.	n.d.	n.d.	203.2
S8$_r$	2.58	0.53	-0.13	1.00	n.d.	n.d.	n.d.	n.d.	n.d.	426.9
S27$_r$	2.49	0.68	-0.29	1.27	n.d.	n.d.	n.d.	n.d.	n.d.	590.0
S18$_r$	2.61	0.99	0.10	1.45	n.d.	n.d.	n.d.	n.d.	n.d.	117.1
S24$_r$	1.53	0.95	0.26	2.07	97.2	0.0	2.8	0.0	0.0	492.7
S14$_r$	2.76	0.52	0.04	0.80	93.7	6.3	0.0	0.0	0.0	474.9
S23$_y$	1.82	0.74	0.26	1.06	83.2	10.6	5.2	1.0	0.0	322.5
S21$_y$	1.84	0.96	0.01	1.49	88.2	6.9	3.5	1.4	0.0	95.76
S16$_y$	3.01	0.63	-0.09	1.08	89.0	9.5	0.0	1.5	0.0	336.5
S17$_y$	2.67	0.42	0.00	0.74	n.d.	n.d.	n.d.	n.d.	n.d.	151.2
S12$_y$	1.79	0.95	0.53	2.51	n.d.	n.d.	n.d.	n.d.	n.d.	137.5
S3$_y$	1.78	0.67	0.38	1.03	87.7	7.8	4.5	0.0	0.0	312.1
S9$_y$	2.17	0.91	-0.17	0.88	92.7	0.0	7.3	0.0	0.0	161.2
S20$_y$	3.20	0.66	-0.20	1.65	n.d.	n.d.	n.d.	n.d.	n.d.	98.13
S7$_y$	1.43	0.80	0.03	1.30	n.d.	n.d.	n.d.	n.d.	n.d.	406.2
S4$_y$	1.99	0.71	0.25	0.77	n.d.	n.d.	n.d.	n.d.	n.d.	294.5
S19$_y$	1.47	0.97	0.24	2.78	84.0	5.0	6.4	4.6	0.0	56.21
S6$_y$	1.10	0.82	0.23	0.95	n.d.	n.d.	n.d.	n.d.	n.d.	87.5
S15$_y$	1.99	0.71	0.24	0.77	n.d.	n.d.	n.d.	n.d.	n.d.	271.7
S2$_w$	2.53	0.67	-0.13	1.90	62.5	0.0	2.0	1.0	34.5	31.25
S11$_w$	2.56	0.62	-0.10	1.59	65.0	0.0	6.3	0.0	28.8	41.23
S1$_w$	2.35	0.73	-0.22	2.51	64.3	0.0	2.9	0.9	31.9	44.26
S5$_w$	2.79	0.60	0.29	0.89	66.1	0.0	0.0	0.0	33.9	30.03
S13$_w$	2.55	0.74	-0.09	1.03	73.9	0.0	3.3	0.6	22.2	82.34

[a] The subscripts r, y, and w next to the sample label point out colors relatively reddish, yellowish, and whitish, respectively.

[b] Q: Quartz, Fds: Feldspars, Ca: Calcite, Do: Dolomite, Gy: Gypsum, n.d.: not determined.

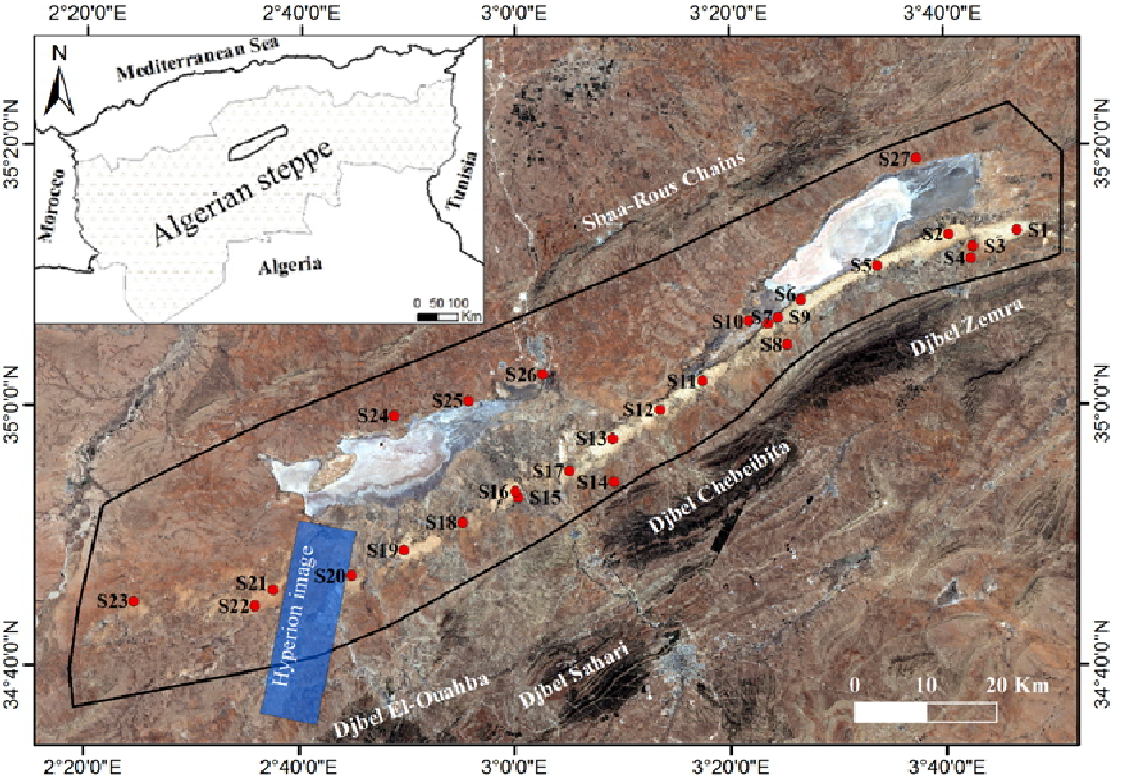
2°20'0"E
2°40'0"E
3°0'0"E
3°20'0"E
3°40'0"E
35°20'0"N
35°0'0"N
34°40'0"N
N
Mediterranean Sea
Morocco
Algerian steppe
Tunisia
Algeria
0 50 100
Km
Shaa-Rous Chains
Djbel Zemra
Djbel Chebeibita
Djbel Sahari
Djbel El-Ouahba
Hyperion image
S1
S2
S3
S4
S5
S6
S7
S8
S9
S10
S11
S12
S13
S14
S15
S16
S17
S18
S19
S20
S21
S22
S23
S24
S25
S26
S27
0 10 20 Km

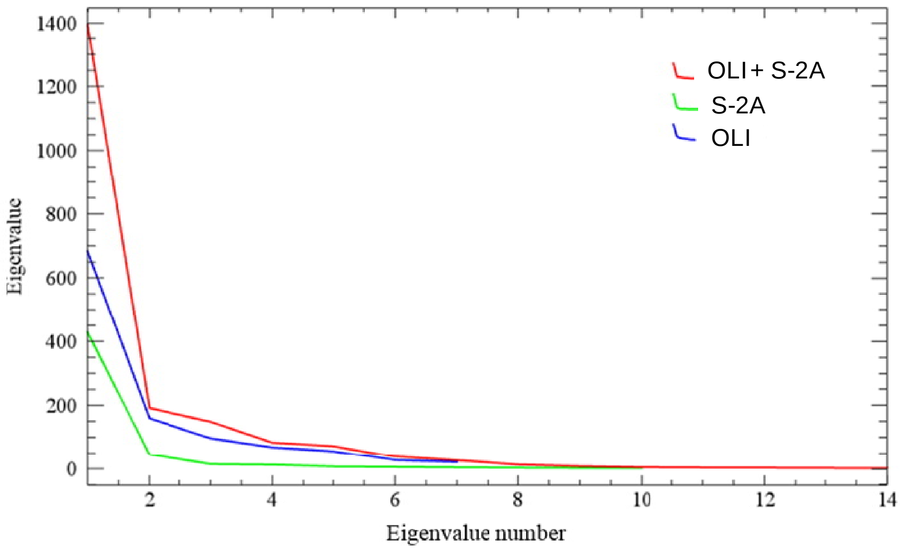
1400
1200
1000
800
600
400
200
0
Eigenvalue
2
4
6
8
10
12
14
Eigenvalue number
OLI+ S-2A
S-2A
OLI

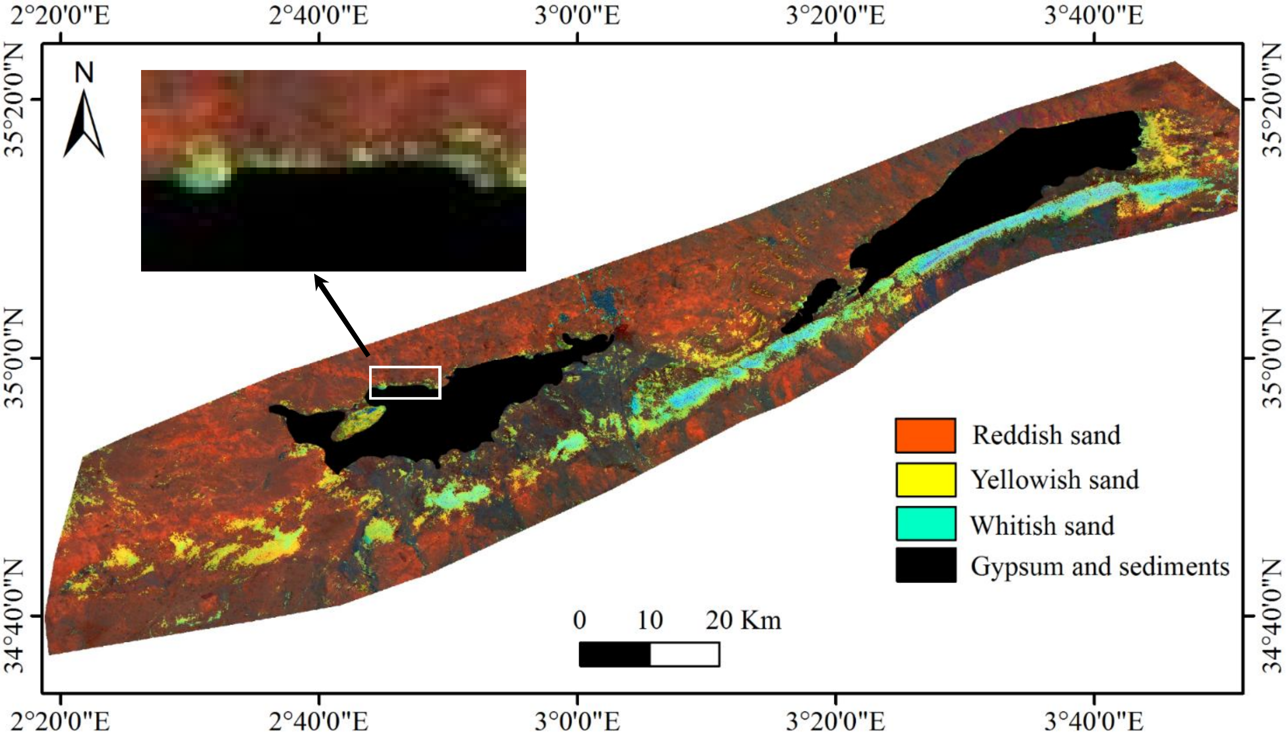
2°20'0"E
2°40'0"E
3°0'0"E
3°20'0"E
3°40'0"E
35°20'0"N
35°0'0"N
34°40'0"N
N
Reddish sand
Yellowish sand
Whitish sand
Gypsum and sediments
0
10
20 Km

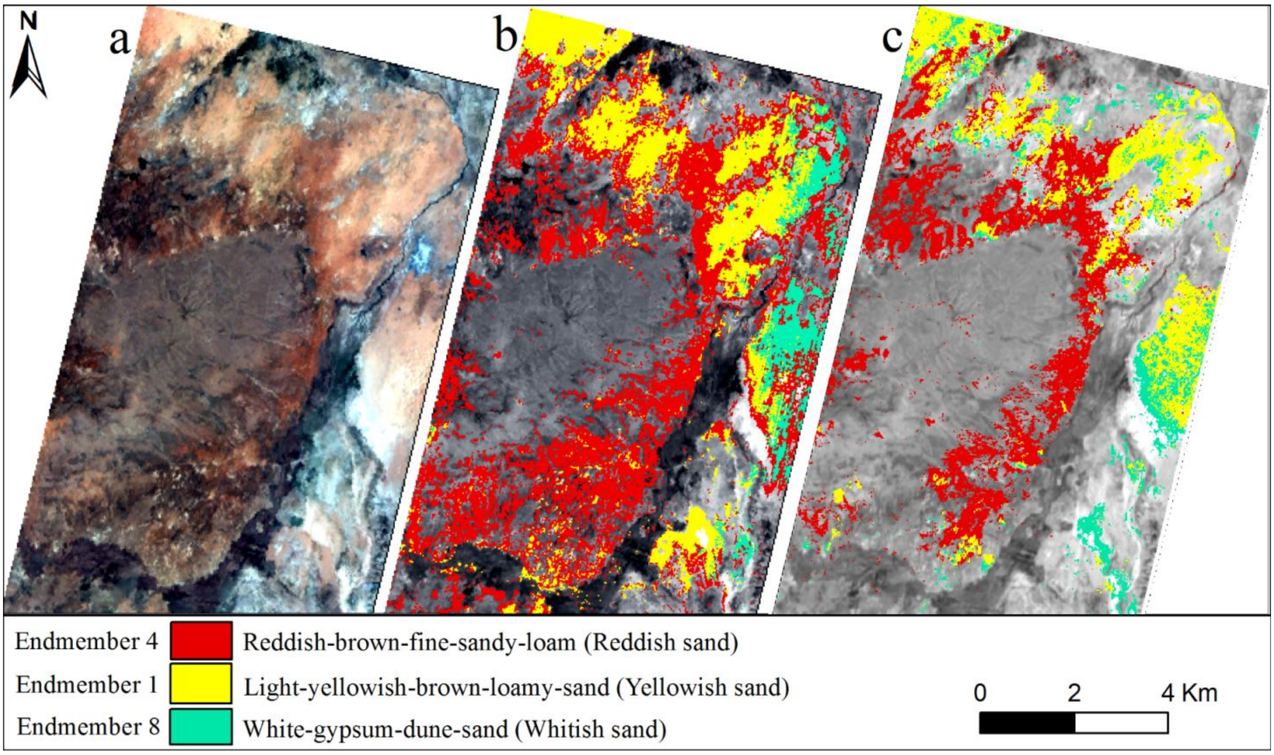
N
a
b
c
Endmember 4
Reddish-brown-fine-sandy-loam (Reddish sand)
Endmember 1
Light-yellowish-brown-loamy-sand (Yellowish sand)
Endmember 8
White-gypsum-dune-sand (Whitish sand)
0
2
4 Km

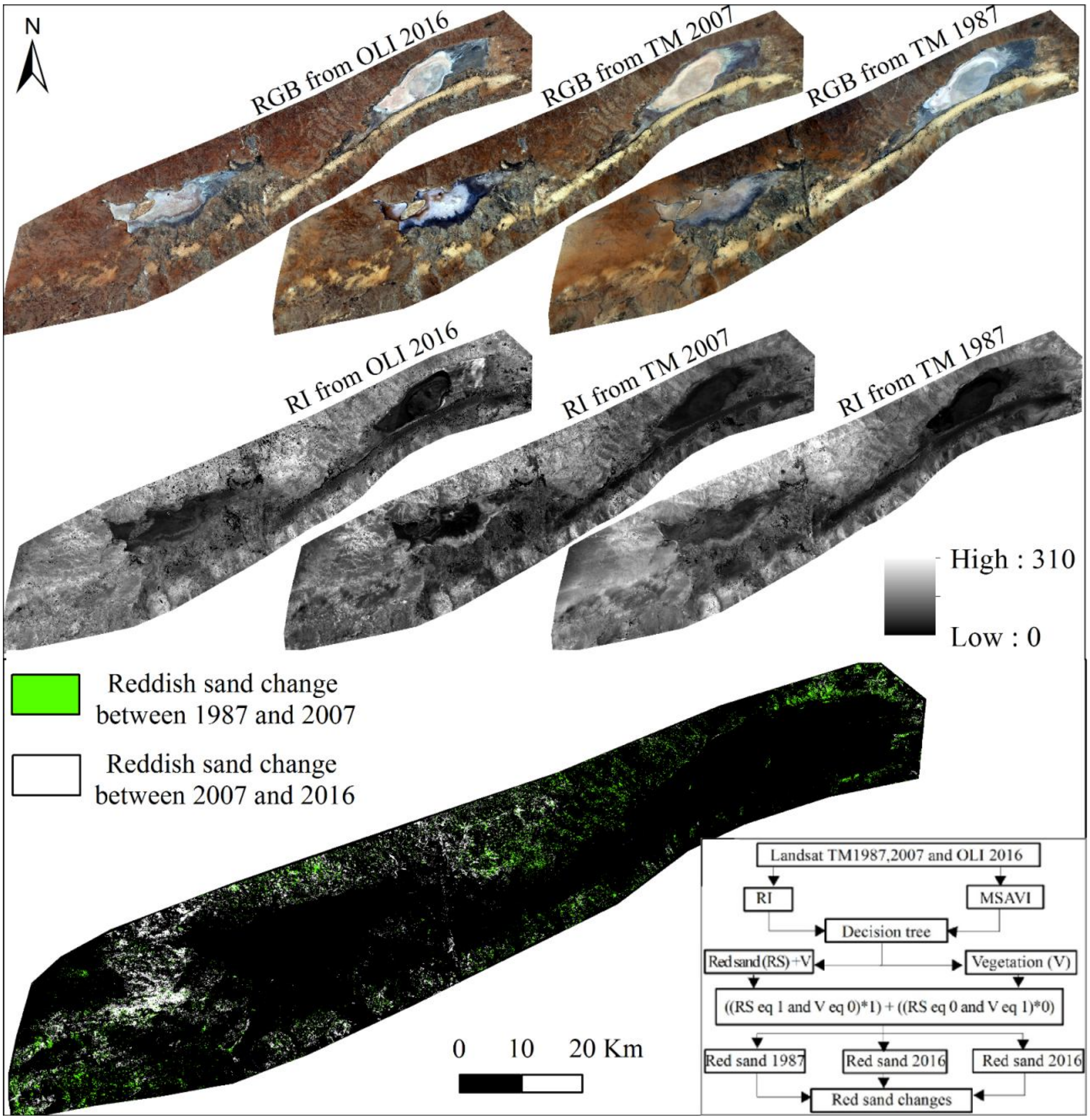
N
RGB from OLI 2016
RGB from TM 2007
RGB from TM 1987
RI from OLI 2016
RI from TM 2007
RI from TM 1987
High : 310
Low : 0
🟩 Reddish sand change between 1987 and 2007
☐ Reddish sand change between 2007 and 2016
0 10 20 Km
Landsat TM1987,2007 and OLI 2016
RI
MSAVI
Decision tree
Red sand (RS) +V
Vegetation (V)
((RS eq 1 and V eq 0)*1) + ((RS eq 0 and V eq 1)*0)
Red sand 1987
Red sand 2016
Red sand 2016
Red sand changes

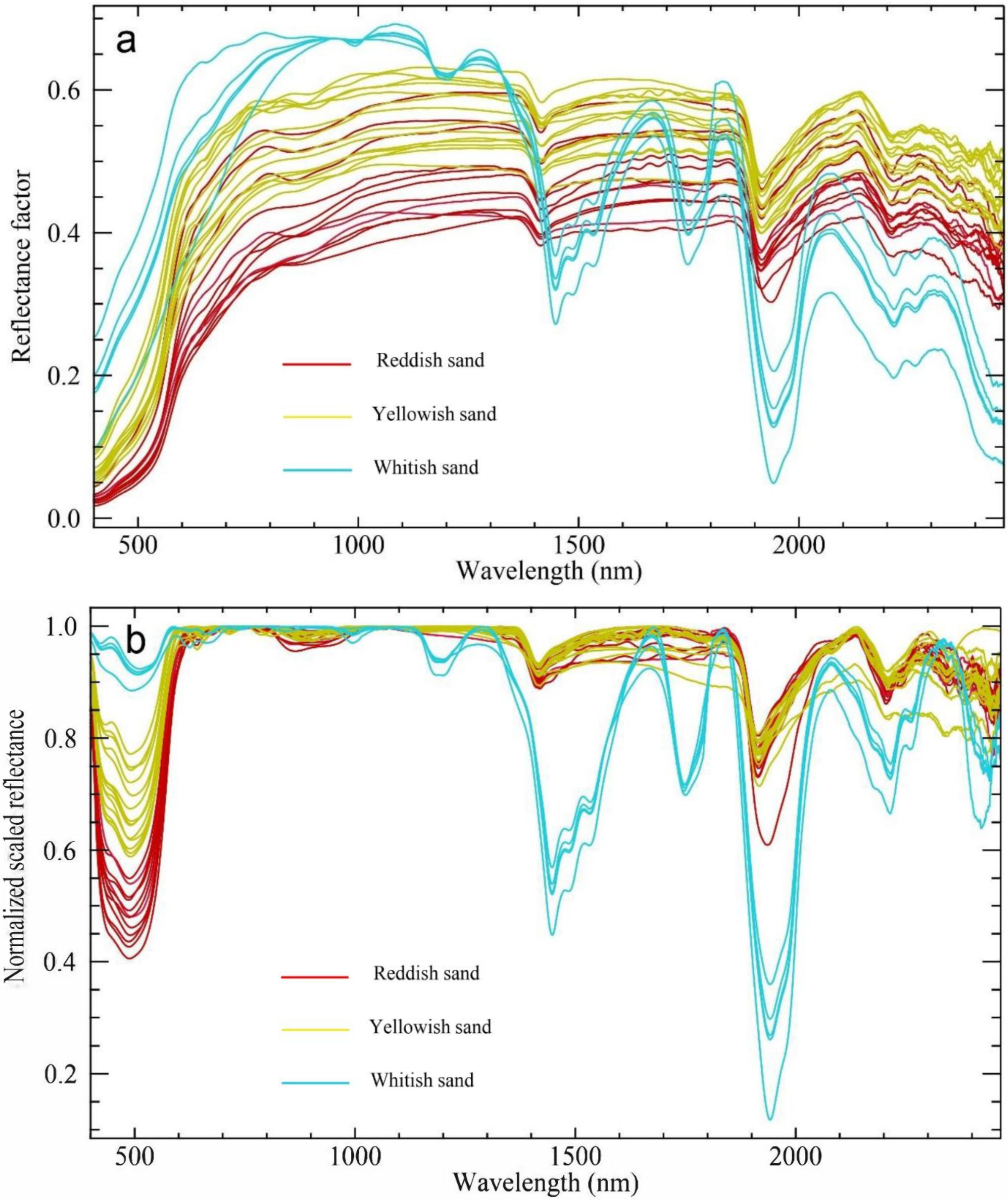
a
Reflectance factor
0.0
0.2
0.4
0.6
500
1000
1500
2000
Wavelength (nm)
Reddish sand
Yellowish sand
Whitish sand
b
Normalized scaled reflectance
0.2
0.4
0.6
0.8
1.0
500
1000
1500
2000
Wavelength (nm)
Reddish sand
Yellowish sand
Whitish sand

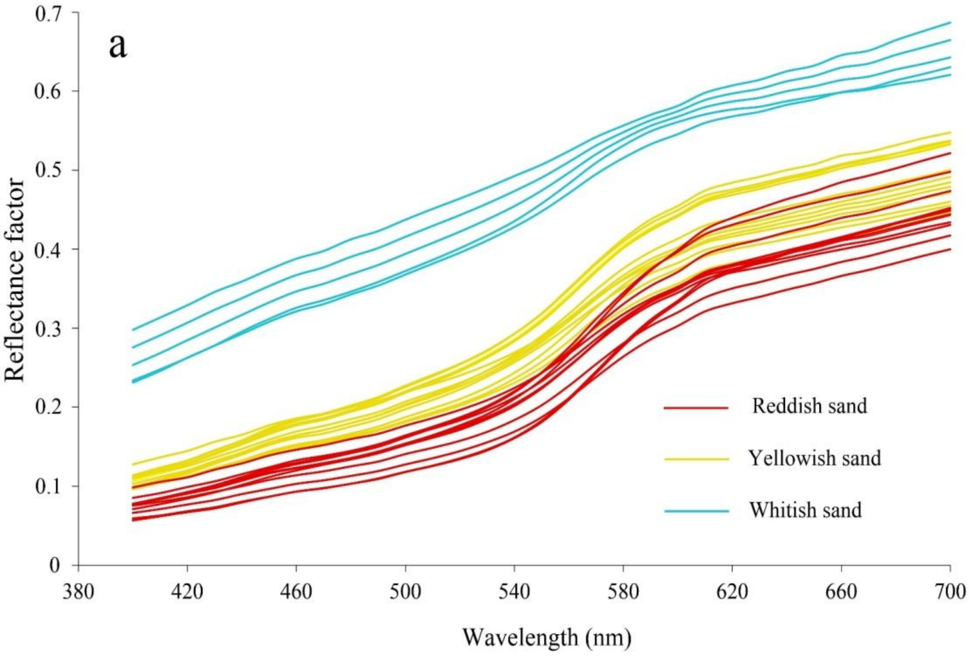
a
Reflectance factor
0.7
0.6
0.5
0.4
0.3
0.2
0.1
0
380
420
460
500
540
580
620
660
700
Wavelength (nm)
Reddish sand
Yellowish sand
Whitish sand

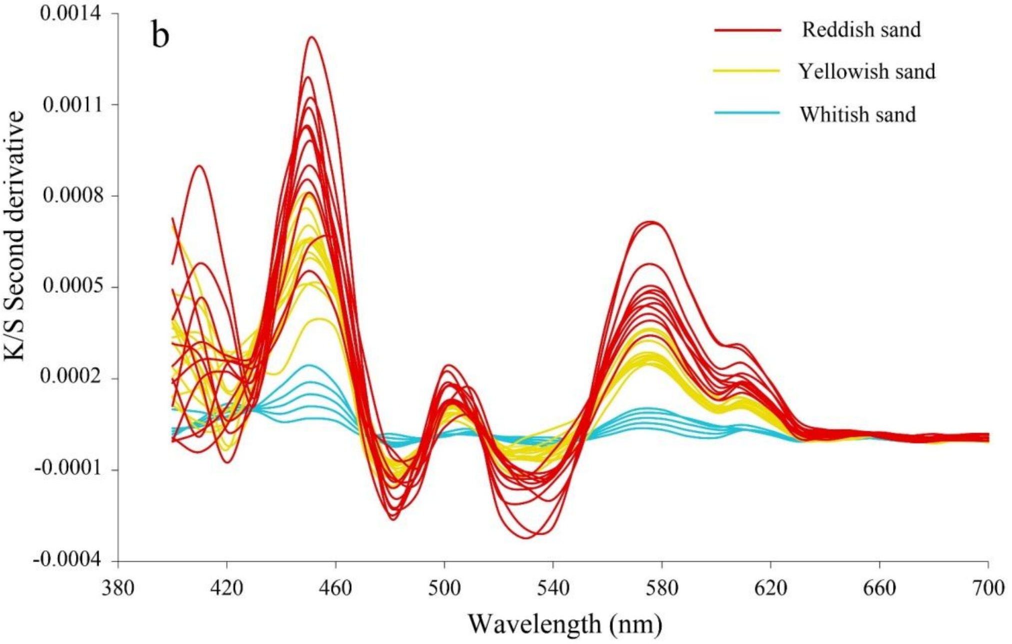
b
K/S Second derivative
0.0014
0.0011
0.0008
0.0005
0.0002
-0.0001
-0.0004
380
420
460
500
540
580
620
660
700
Wavelength (nm)
Reddish sand
Yellowish sand
Whitish sand

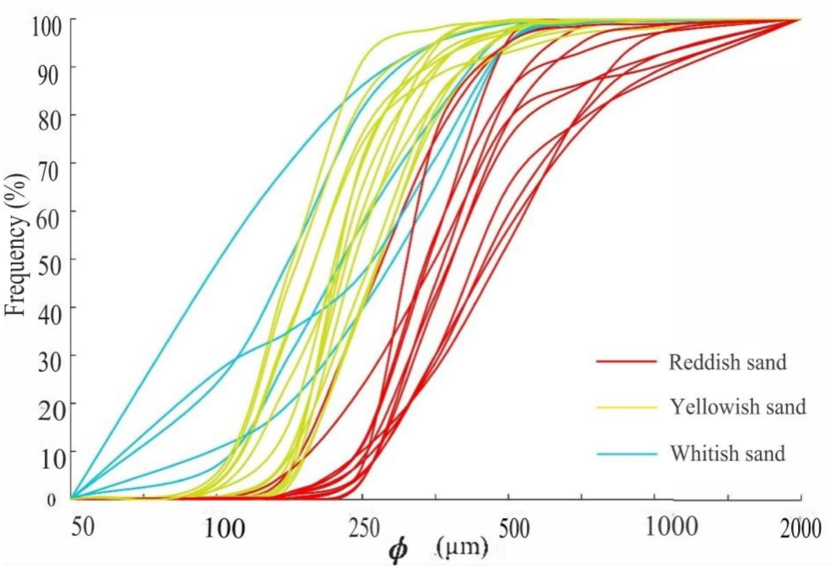
Frequency (%)
100
90
80
70
60
50
40
30
20
10
0
50
100
250
500
1000
2000
ϕ (μm)
Reddish sand
Yellowish sand
Whitish sand

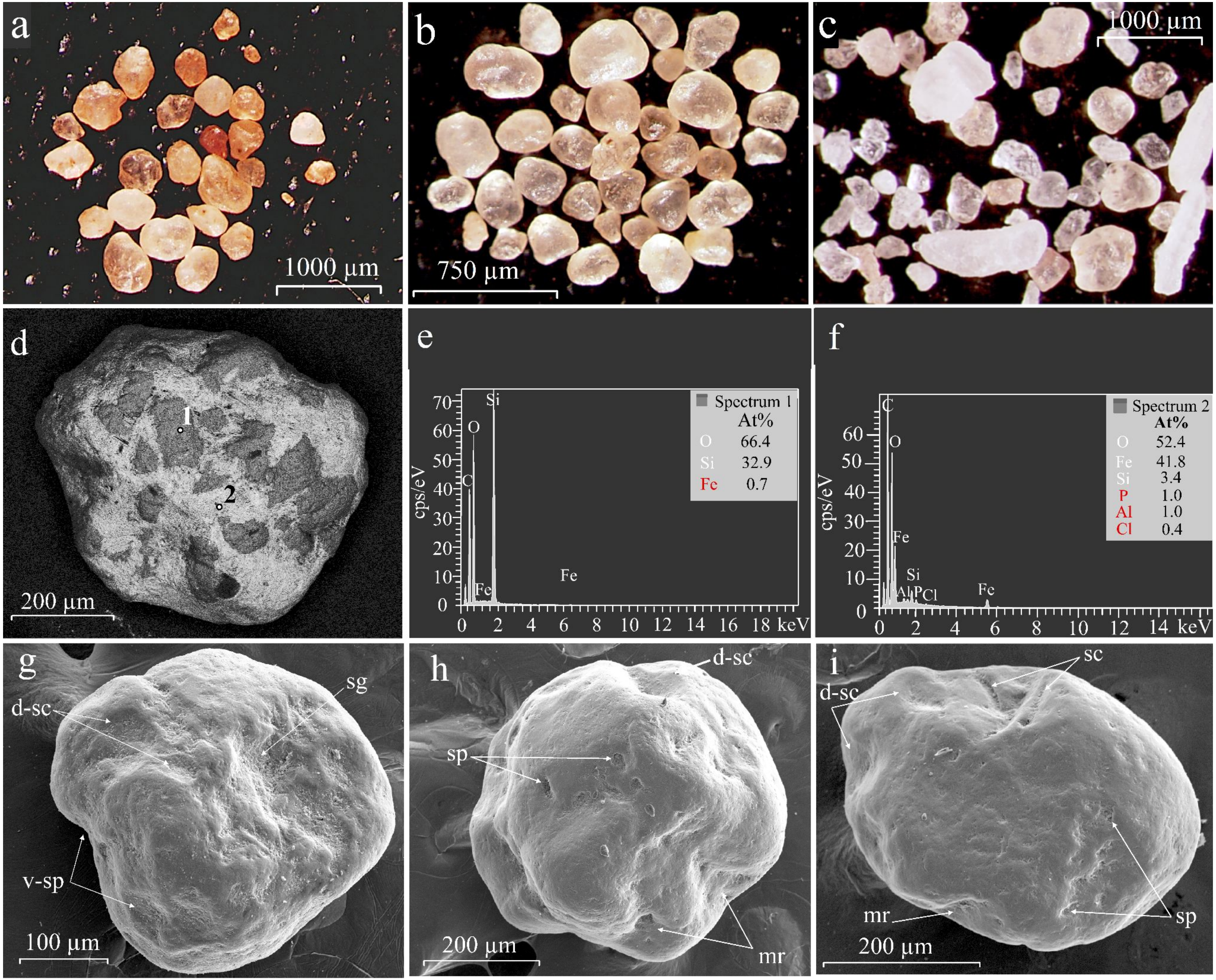
a
1000 µm
b
750 µm
c
1000 µm
d
1
2
200 µm
e
Spectrum 1
At%
O 66.4
Si 32.9
Fe 0.7
cps/eV
0 10 20 30 40 50 60 70
O
Si
C
Fe
Fe
0 2 4 6 8 10 12 14 16 18 keV
f
Spectrum 2
At%
O 52.4
Fe 41.8
Si 3.4
P 1.0
Al 1.0
Cl 0.4
cps/eV
0 10 20 30 40 50 60
C
O
Fe
Si
Al
P
Cl
Fe
0 2 4 6 8 10 12 14 keV
g
d-sc
sg
v-sp
100 µm
h
d-sc
sp
mr
200 µm
i
sc
d-sc
mr
sp
200 µm

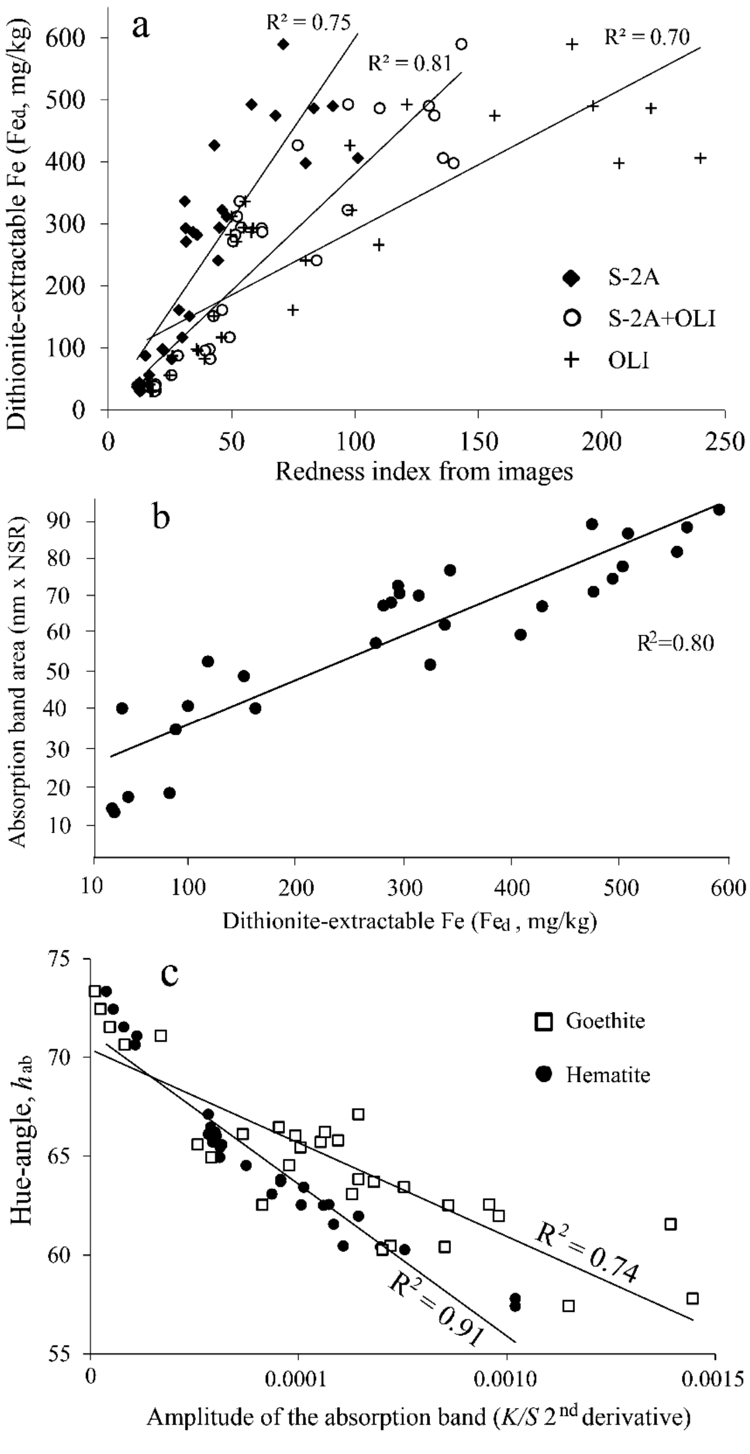
a
R² = 0.75
R² = 0.81
R² = 0.70
S-2A
S-2A+OLI
OLI
Dithionite-extractable Fe (Fed, mg/kg)
0
100
200
300
400
500
600
0
50
100
150
200
250
Redness index from images
b
R²=0.80
Absorption band area (nm x NSR)
10
20
30
40
50
60
70
80
90
10
100
200
300
400
500
600
Dithionite-extractable Fe (Fed , mg/kg)
c
Goethite
Hematite
R² = 0.74
R² = 0.91
Hue-angle, hab
55
60
65
70
75
0
0.0001
0.0010
0.0015
Amplitude of the absorption band (K/S 2nd derivative)

Figure captions

Fig. 1. Location of the study area and sampling points. The background image is produced by assigning the bands b4, b3, and b2 of the Sentinel-2A image to RGB color. The Hyperion image area is also displayed.

Fig. 2. Minimum-Noise-Fraction (MNF) eigenvalue plot from multispectral bands of the Landsat OLI (b1 to b7) and Sentinel-2A (b2 to b8a, b11, and b12) images processed individually and as a combined solution of 14 bands (7 OLI bands + 7 S-2A bands; see Methods).

Fig. 3. Mixture-Tuned-Matched-Filtering (MTMF) sand map from combined OLI + S-2A bands showing the spatial distribution of the endmembers reddish-brown fine sandy loam (reddish sand), light-yellowish-brown loamy sand (yellowish sand), and white gypsum dune sand (whitish sand). Gypsum, dry sediments, and wet sediments are in the sabkhas.

Fig. 4. Natural color composite of the Hyperion image (a) and the resulting Spectral-Angle-Mapper (SAM) sand map (b). The latter can be compared with the MTMF sand map derived from OLI + S-2A data in the Hyperion image area (c).

Fig. 5. Redness index (RI) maps from Landsat TM images of 1987 and 2007 using the bands b1 (450-520 nm), b2 (520-600 nm) and b3 (630-690 nm), and from Landsat OLI images of 2016 using the bands b2 (452-512 nm), b3 (533-590 nm) and b4 (636-673 nm). Considering RI > 65 as reddish sand, a map also shows the spatiotemporal changes in the distribution of reddish sand.

Fig. 6. Visible and near-infrared spectra of the sand samples as obtained in the laboratory before (a) and after applying the continuum removal algorithm (b).

Fig. 7. Reflectance spectra in the visible region of the sand samples (a) and second derivative of the Kubelka-Munk function (b).

Fig. 8. Cumulative curves of the grain size distribution in the sand fraction (0.05-2.0 mm) of the samples.

Fig. 9. Morphology of sand grains. Binocular magnifying-glass micrographs of grains from the reddish sample S25 (a), yellowish sample S7 (b), and whitish sample S13 (c). Scanning electron micrographs of a quartz grain with surface Fe-oxide coatings from S26 (d) and EDX pinpoint spectra (e, f), as well as quartz grains deferrified by acid treatment from the samples S26 (g), S16 (h), and S2 (i). In the last three, silica globules (sg), V-shaped percussion cracks (v-sp), dish-shaped concavities (d-sc), meandering ridges (mr), solution pits (sp), and solution crevasses (sc) can be observed on their surface.

Fig. 10. Relationship of the Fe-oxide content with the redness index measured in satellite images (a) and with the area of the absorption band at ~500 nm measured in the continuum removal spectrum (b). The CIELAB hue-angle is also regressed on the amplitude of the 2nd derivative curve of the Kubelka-Munk function between 420 nm and 450 nm for goethite and between 540 nm and 580 nm for hematite (c).